Desalination and Water Treatment
www.deswater.com

doi: 10.1080/19443994.2015.1006261

56 (2015) 1121–1139
October

Taylor & Francis
Taylor & Francis Group

Response surface modeling and optimization of microcystin-LR removal from aqueous phase by polyacrylamide/sodium alginate–montmorillonite superabsorbent nanocomposite

Zhiyuan Wang, Chao Wang, Peifang Wang*, Jin Qian, Jun Hou, Yanhui Ao

Key Laboratory of Integrated Regulation and Resource Development on Shallow Lakes, Ministry of Education, College of Environment, Hohai University, 1# Xikang Road, Nanjing 210098, China, Tel. +86 025 83787332;
email: zhiyuan.wang1988@hotmail.com (Z. Wang), Tel. +86 025 83786971; email: cwang@hhu.edu.cn (C. Wang), Tel. +86 025 83787930; email: pfwang2005@hhu.edu.cn (P. Wang), Tel. +86 025 83787332; emails: hhuqj@hhu.edu.cn (J. Qian), hhuhjyhj@126.com (J. Hou), andyao@hhu.edu.cn (Y. Ao)

Received 20 October 2014; Accepted 4 January 2015

ABSTRACT

The adsorptive removal of the most commonly occurring cyanobacterial toxin microcystin–LR by polyacrylamide/sodium alginate-modified montmorillonite (PAM/SA-MMT) superabsorbent nanocomposite was investigated through the HPLC/UV system. The process of PAM/SA-MMT preparation and MC-LR adsorption was characterized by scanning electron microscopy, energy dispersive X-ray microanalysis, X-ray diffraction analysis, and Fourier transform infrared spectroscopy analysis. With the application of Box–Behnken statistical experimental design combined with Response surface methodology, the quadratic statistical model was established to predict the interactive effects of pH, weight ratio (wr) of AM to SA, and weight content (wt) of MMT on MC-LR adsorption and to optimize the main controlling parameters. The maximum adsorption capacity was observed with pH 2.5–4.5, wr 55–65, and wt3–5%. The MC-LR adsorption capacity of PAM/SA-MMT increased with increase in temperature from 10 to 40°C. Kinetics were consistent with Pseudo models and revealed that the sorption process could reach the equilibrium within 80 min and involved several different rate-controlling kinetic stages. The Langmuir isotherm model predicted that the theoretical maximum adsorption capacity of PAM/SA-MMT was 32.66 mg g^{-1}. Over 85% adsorption and 80% desorption could be achieved after five regeneration cycles and the recovery of MC-LR reached 92.8% without ionic effect. PAM/SA-MMT superabsorbent nanocomposite was determined as effective, economic, and environmentally benign for MC-LR removal on a large-scale application.

Keywords: Superabsorbent nanocomposite; Polyacrylamide; Microcystin-LR; Adsorption; Response surface; Box–Behnken

1. Introduction

In recent years, blue–green algae blooms have been reported in many natural water bodies all over the world as the most visible symptom of eutrophication caused by excessive supply of nutrients. During the algal blooms, cyanotoxins, mainly microcystins (MCs) are released into aquatic systems by the natural biological process of artificial induction and cell lysis [1].

*Corresponding author.

The acute lethal toxicity of MCs can exert devastating effects on human internal organs and induce tumor-promoting activity through the inhibition of protein phosphatases [2,3]. Among more than 80 molecular variants of MCs, MC-LR has been identified as the most fatal and commonly occurring variant so far [4,5]. The World Health Organization recommended a provisional safety guideline of 1.0 $\mu g\,L^{-1}$ for MC-LR in drinking water [6].

MC-LR is very stable in water and resistant to most traditional water treatment methods [7]. Several removal strategies for MC-LR by adsorbents have been explored until now due to their easy operation, economical advantages, and low-energy cost. Many researchers have discovered that clay minerals, sediments, activated carbon, and their derivative products (carbon nanotubes, graphene oxide, etc.) are attractive options as adsorbents to eliminate MC-LR [6,8–11], although the industrial applications were seriously restricted owing to high production cost or limited adsorption capacity.

Superabsorbent polymers (SAP) composite appears to be a cost-effective solution for MC-LR adsorptive removal. The porous network structure and the ionic functional groups of SAP ensure that the MC-LR molecules can diffuse and bind through them. The organic modification of SAP composites based on clays, polysaccharides, and synthetic polymers is attracting increasing interest because these water treatment materials could also improve the adsorption properties of SAP composites in aqueous media [12–14]. All components of the composite are biodegradable, easy to acquire, and convenient for grafting polymerization [15]. The traditional SAP is usually prepared via *in situ* intercalative grafting copolymerization under protection of nitrogen [16]. We therefore prepared the SAP/clay composite with nano-sized polysaccharide-modified clays (designated as two-step method). The reaction was carried out under normal atmospheric condition, which demonstrated the brevity and simplicity required for practical industrial operation [17]. However, to our best knowledge, it would be the first time for SAP/clay nanocomposite to be applied on the adsorption process of MC-LR and systematically investigated.

Polyacrylamide (PAM) was chosen as the synthetic polymer component of SAP. PAM is salt-resisting, nontoxic, and relatively inexpensive compared with other polyacrylic products, hence it has been widely used as a flocculant [18,19]. Its nonionic groups ($–CONH_2$) could be saponified and transferred to ionic groups ($–COONa^+$), which might improve the adsorption ability [17].

Sodium alginate (SA) is one of the most commonly used biopolymers for removal of aqueous pollutants as this polysaccharide component is cheap, biodegradable, and efficient [20]. Inspired by the fact that organic modification of clays could improve their adsorptive performance and ion exchange properties, SA was applied as the clay modifier because of its good adsorption capacity and salt-resisting property [21,22].

Nano-sized clays are introduced into the preparation of this inorganic–organic SAP composite to improve its hydrogel strength, to enhance its swelling ability, and to reduce the production cost [23]. Montmorillonite (MMT) is a natural clay material whose basic structural unit contains a sandwiched octahedrally coordinated layer of aluminum ions surrounded by two tetrahedrally coordinated loose layers of silicon ions [24]. MMT K10, a type of synthetic bentonite clay activated with mineral acid, has been widely applied as an active catalyst [25]. Nano-sized MMT (NMMT) K10, which is economically accessible, regenerative, and non-corrosive for eventual disposal, is thus a potential cost-effective adsorbent for large-scale industrial applications. Compared with natural granular MMT, the modified NMMT K10 with polysaccharide is more uniformly dispersed, and has higher specific surface area and weaker bonds between layers, which provides better cleavage and more available sorption sites within its interlayer space for micro-pollutant molecules [26,27]. As an efficient inorganic exchanger with a stable microporous structure, different feed contents of NMMT K10 in nanocomposites could influence the chemical environment of the modified composites and hence the adsorption properties [28].

Statistically based Box–Behnken experimental design and Response surface methodology (RSM) has been widely applied with the aim to optimize the performance of nanocomposite synergically affected by multiple environmental controlling variables [29,30]. RSM has proved to be effective and is frequently used to identify the interaction effects and predict the values of significant variables from a large number of potential variables with the minimum amount of optimized testing [31,32]. However, no modeling attempts have been made to adopt the full range of RSM to determine the interaction effects of combined controlling parameters on MC-LR uptake by SAP composite and to optimize the operational conditions for the maximum uptake of MC-LR from aqueous solution while permitting reduction in the actual number of combination experiments to be performed.

In this work, the adsorption mechanism of MC-LR toxin onto PAM based SAP intercalated with SA modified MMT (PAM/SA-MMT) was studied. Scanning

electron microscopy (SEM), energy dispersive X-ray (EDX) microanalysis, X-ray diffraction (XRD) analysis, and Fourier transform infrared spectroscopy (FT-IR) analysis were used to characterize the structure and surface morphology of PAM/SA-MMT. By performing a batch of experiments designed with the Box–Behnken model, we established the three-dimensional (3D) numerical response surface model and assessed the MC-LR adsorption on PAM/SA-MMT affected by the operating parameters of pH, weight ratio (wr) of AM to SA, and weight content (wt) of MMT K-10. The adsorption kinetics and the isotherm modeling related to the physical and chemical properties of PAM/SA-MMT were investigated. The regeneration capacity of PAM/SA-MMT was also examined by a batch of adsorption/desorption cycling studies.

2. Materials and methods

2.1. Chemicals and materials

Nano-sized MMT K-10 with purity 95% was supplied by Liaoyuan 4S-tech Co., Ltd., Nanjing, China. The cationic exchange capacity of MMT K-10 is 96.3 mequiv/100 g. Acrylamide (AM), SA, ammonium persulfate (APS, as the reaction initiator), and N,N-methylenebisacrylamide (NMBA, as the crosslinker) were all analytical grade and supplied from Aladdin Reagent Co., Ltd., Shanghai, China. MC-LR standard was purchased from Agent Technology (Switzerland) and stored below −25℃. HPLC-grade methanol and formic acid were obtained from Tedia (OH, USA) and Merck (Germany), respectively. Milli-Q deionized water (18 MΩ) was used in all experiments and obtained through a Milli-Q water purification system (Millipore, Bedford, MA, USA).

2.2. Preparation of PAM/SA-MMT superabsorbent nanocomposite

The preparation of PAM/SA-MMT consisted of two steps, which is similar to the two-step preparation method of other reported superabsorbent nanocomposites [33]. A series of SA modified MMT composites with different feed compositions of MMT and SA were prepared according to the following procedure. The feed compositions of MMT and SA were calculated according to the wr of AM to SA and the wt of MMT listed in the Box–Behnken experimental matrix:

$$m_{SA} = m_{AM}/wr \quad (1)$$

$$m_{MMT} = (m_{AM} + m_{SA}) \times wt \quad (2)$$

where m_{AM} is the content of AM, m_{SA} is the content of SA, and m_{MMT} is the content of MMT. Nano-sized MMT K-10 suspension was prepared with a certain amount (m_{MMT}) of MMT dispersed in 100 mL deionized water using a magnetic stirrer equipped with a thermostat (Guohua 85-2, China) for 2 h at room temperature. Similarly, a certain amount (m_{SA}) of SA was diluted in 100 mL deionized water. The SA solution was added to the MMT suspension and agitated vigorously for 2 h at 70℃. The mixture was dried in an oven at 70℃ to a constant weight, grounded and milled through a 300 mesh screen.

The PAM based PAM/SA-MMT nanocomposite was then synthesized. An 8 g AM was totally dissolved in 100 mL deionized water. The previously prepared powder of SA-modified MMT was added to the AM monomer solution and agitated vigorously for about 8 h till it was well dispersed. About 20 mg APS and 15 mg NMBA were added to the mixed solution of AM and SA modified MMT. The mixture was agitated and heated to 70℃ in a water bath for 2 h, followed by the addition of 10 mL 40% NaOH solution, and then the primary product was heated to 90℃ to be saponified for 2 h. After the saponification, we washed the formed nanocomposite for several times with deionized water until the pH of the supernatant fluid reached 7.0. The purified product was dried in an oven at 70℃ for 12 h. The dried gel was milled and screened to 300 mesh. All samples used for test had a particle size of <0.3 mm.

2.3. MC-LR quantification

The concentrations of MC-LR in the samples were determined by the HPLC system [10]. The HPLC system comprised of a Waters Alliance e2695 separations module (Waters Corporation, Milford, MA, USA), a Waters 2489 UV/Visible detector, a Waters 2998 photodiode array detector, an inline vacuum degasser, a quaternary mixing pump, a thermostated autosampler, and a heated column compartment. The spectrophotometric system was fully enclosed to ensure high spectral resolution and accuracy, and the wavelength was set to 238 nm. The separation was achieved on an XBridge LC C18 5 μm, 4.6 × 150 mm column (XBridge Systems, Inc., Mountain View, CA, USA). The injection volume was 10 μg L^{-1} with a flow rate of 0.6 mL min^{-1}. The mobile phase consisted of 0.1% formic acid in water (solvent A, 40%) and 0.1% formic acid in HPLC-grade methanol (solvent B, 60%). The standard curve ($R^2 > 99.5\%$) was obtained for MC-LR concentrations ranging from 5 to 1,000 μg L^{-1} to ensure minimal system error.

2.4. Characterization of PAM/SA-MMT superabsorbent nanocomposite

SEM and EDX analysis were performed for morphological analyses with a SEM (Hitachi S-4800, Japan) attached with an EDX spectrometer. All samples were dried and coated with gold to enhance the electron conductivity before the scanning process. The images of SA-MMT and PAM/SA-MMT were captured with an electron beam (high accelerating voltage of 20 kV) at a 45° tilt on the left side. EDX analysis was used to analyze the occurrence of elements in the specimens.

XRD measurements were performed using an X-ray power diffractometer with Cu anode ($\lambda = 0.154$ nm) at a generator voltage of 40 kV and a generator current of 100 mA, scanning from 5° to 22° at 3° min^{-1} (Bruker® AXS D8 Advance, Germany).

To obtain the FT-IR spectra, PAM/SA-MMT samples before and after MC-LR adsorption were dried overnight at 70°C. PAM/SA-MMT (0.1 g) was mixed with KBr (0.9 g) and pressed into a tablet form with the aid of a bench press. The resulting transparent pellet was used to analyze the surface functional groups by IR spectroscopy (Bruker Tensor 27, Germany) scanned between 4,000 and 400 cm^{-1} at a resolution of 4 cm^{-1}.

Through surface charge titration, we detected the zero point of charge (pH_{pzc}) representing the pH where the surface ionic groups were neutralized and the surface was effectively uncharged [34]. The pH_{pzc} (pH point of zero charge) of the superabsorbent was determined by the solid addition method [35]: 0.01 M NaCl was placed in a closed Erlenmeyer flask and its pH was adjusted to a value between 2 and 12 by 0.1 M HCl or NaOH. A fixed amount of PAM/SA-MMT sample was added under agitation at 25°C and the final pH values of the various buffer solutions were measured and plotted after 2 d. The pH_{pzc} is the point where the curve pH_{final} intersects with $pH_{initial}$.

2.5. Box–Behnken experimental design: RSM approach

The Box–Behnken model was used for the experimental design to evaluate the interactive effects of the significant operating parameters and to optimize the adsorption of MC-LR on PAM/SA-MMT. The three main controlling parameters pH (2–12), wr of AM to SA (20–80), and wt of MMT (1–20%) were chosen as model variables to study their interaction effects on the PAM/SA-MMT adsorption capacity for MC-LR. Each independent actual parameter was varied over three coded levels (−1, 0, +1), which composed the batch experimental design matrix derived from the Box–Behnken design summarized in Table 1. The amounts of MC-LR removed by PAM/SA-MMT (μg L^{-1}) under different experimental combinations based on this matrix were estimated as the model responses.

The true value of each determined variable i was coded as follows:

$$x_i = \frac{X_i - X_{ci}}{\Delta X_i}, \quad i = 1,\ 2,\ 3, \ldots,\ k \tag{3}$$

where x_i is the coded level, X_i is the real value of an independent variable, X_{ci} is the real value of an independent variable at the central point, and ΔX_i is the step change of variable i.

These independent factors were represented as process variables in a quantitative form:

$$Y = f(A, B, C) \tag{4}$$

where Y is the predicted response of MC-LR removal, and A (pH), B (wr of AM to SA), and C (wt of MMT) are the coded levels of the actual variables.

The response values were approximated by a suitable linear polynomial first, then by the quadratic, cubic, and higher order polynomial. In the system with curvature, the second-order polynomial in the form of a quadratic model showed the best fit with our experimental data:

$$Y = k_0 + k_1A + k_2B + k_3C + k_{12}AB + k_{13}AC + k_{23}BC + k_{11}A^2 + k_{22}B^2 + k_{33}C^2 \tag{5}$$

where k_{ij} are the estimated coefficients of the equation. A total of 16 different experimental combinations (including four replicates of the center point for error estimation) was designed for calculation of the 10 coefficients of the second-order polynomial equation to approximate the experimental values, which were derived from the standard Box–Behnken model established by Design Expert® (DX) 8.0.5 (Stat-Ease Inc., Minneapolis, MN, USA). The determination of the complex response surface provided by relatively few combinations of variables was obtained by plotting the expected response values.

2.6. Experimental studies of MC-LR adsorption by PAM/SA-MMT

The influence of pH and temperature on MC-LR uptake was studied by agitating 5 mg of PAM/SA-MMT with 100 mL of 500 μg L^{-1} MC-LR solution under different pH conditions (2–12) and various

Table 1
Box–Behnken design matrix of three variables (pH, wr of PAM to SA, and wt of MMT) along with the experimental responses

	Variables					Variables			
Run	pH	wr PAM/SA	wt% MMT	MC-LR uptake ($\mu g\,L^{-1}$)	Run	pH	wr PAM/SA	wt% MMT	MC-LR uptake ($\mu g\,L^{-1}$)
1	2	20	10.5	411.6	9	7	50	10.5	455.4
2	2	50	1	483.1	10	7	50	10.5	455.4
3	2	50	20	426.3	11	7	80	1	461.3
4	2	80	10.5	455.2	12	7	80	20	390.2
5	7	20	1	412.1	13	12	20	10.5	387.7
6	7	20	20	389.3	14	12	50	1	436.1
7	7	50	10.5	455.4	15	12	50	20	366.4
8	7	50	10.5	455.4	16	12	80	10.5	397.5

temperature (10–40˚C) at 200 rpm in the thermostated magnetic stirrer for 12 h. The solution pH was adjusted using a pH meter (Mettler-Toledo, FE20 FiveEasy™ pH, Switzerland). The pH at which the peak of MC-LR uptake by PAM/SA-MMT occurs is defined as pH_{max}. The MC-LR removal percentage and the adsorption capacity of PAM/SA-MMT for MC-LR were calculated as follows:

$$R = (1 - C/C_0) \times 100\% \quad (6)$$

$$Q = (C_0 - C)V/M \quad (7)$$

where R is the instantaneous MC-LR removal percentage (%), Q is the adsorption capacity of PAM/SA-MMT for MC-LR ($\mu g\,g^{-1}$), C_0 is the initial MC-LR concentration ($\mu g\,L^{-1}$), C is the instantaneous MC-LR concentration ($\mu g\,L^{-1}$), V is the volume of the solution (mL), and M is the PAM/SA-MMT dose (mg).

The kinetic experiments were conducted at various concentrations of MC-LR ranging from 100 to 500 $\mu g\,L^{-1}$ and at pH_{max} with the superabsorbent dose fixed at 50 $mg\,L^{-1}$. Samples were collected at different predetermined time intervals (every 10 min until 90 min and then every 15 min after 90 min) and the MC-LR remaining in solution was estimated. The adsorption isotherm experiments were conducted with various MC-LR initial concentrations (100–1,000 $\mu g\,L^{-1}$) at pH_{max} with 50 $mg\,L^{-1}$ of PAM/SA-MMT. An agitation time of 12 h was selected to ensure that complete equilibrium of the sorption reaction was achieved.

2.7. Batch adsorption/desorption studies in simulated ionic conditions

Regeneration cycling studies were conducted in simulated ionic water samples to study the reusability of PAM/SA-MMT. With the consideration of practical application, adsorption of MC-LR was studied with the presence of various cations (Na^+, K^+, Mg^{2+}, and Ca^{2+}) and anions (NO_3^-, NO_2^-, PO_4^{3-}, SO_4^{2-}, and Cl^-). The concentration range of ions for simulation was fixed as 0, 25, 50 mg/L, which was based on our previous analysis of fresh water samples from Taihu in China. The simulated water samples were spiked with 100 $\mu g\,L^{-1}$ MC-LR and agitated with 0.5 $g\,L^{-1}$ PAM/SA-MMT at 200 rpm and pH_{max} in the thermostatted magnetic stirrer for 12 h. We separated the adsorbent by centrifugation and analyzed the supernatant water samples containing residual MC-LR separately. The dry-loaded adsorbent was recovered and gently washed with deionized water to remove any unadsorbed toxins [12].

These MC-LR laden adsorbents were stirred using the magnetic stirrer with Erlenmeyer flasks containing deionized water adjusted to pH 2–12 using 0.1 M HCl or NaOH and agitated for 24 h. Desorption was also carried out in a similar manner using acetone, 95% ethanol, methanol, 0.1 M HCl, and 0.1 M NaOH. The desorbates were analyzed for MC-LR content. After desorption, these adsorbents were centrifugated, gently washed with deionized water, and dried at 70˚C for 24 h. The same adsorbents were subsequently agitated with spiked drinking water samples of MC-LR for the next cycle of adsorption/desorption.

3. Results and discussion

3.1. SEM, EDX, XRD and FT-IR analysis of PAM/SA-MMT

The SEM images in Fig. 1(a) and (c) show the morphology of SA-MMT and PAM/SA-MMT. The white particles correspond to nano-sized MMT K-10, and the black opaque background represents the polymer

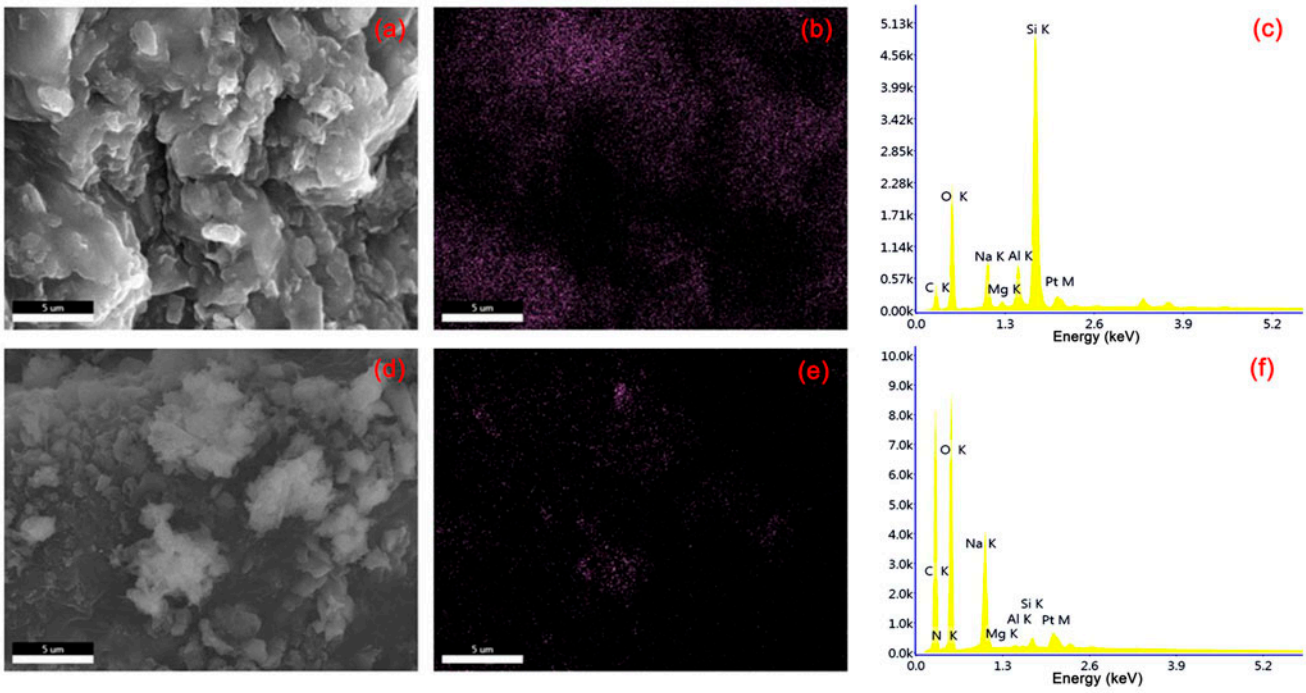

Elements	SA-MMT		PAM/SA-MMT	
	Weight (%)	Atom (%)	Weight (%)	Atom (%)
C	21.60	33.10	41.07	49.88
N	-	-	7.21	7.51
O	37.02	42.59	39.64	36.11
Na	7.09	5.68	9.64	6.11
Mg	0.24	0.18	0.14	0.09
Al	3.40	2.32	0.10	0.05
Si	23.59	15.46	0.18	0.10
Pt	7.05	0.67	2.00	0.15

Fig. 1. SEM, EDX films and EDX spectra of SA-MMT, and PAM/SA-MMT: (a) SA-MMT (SEM), (b) SA-MMT (EDX silicon distribution), (c) SA-MMT (EDX spectrum), (d) PAM/SA-MMT (SEM), (e) PAM/SA-MMT (EDX silicon distribution), (f) PAM/SA-MMT (EDX spectrum); wr = 60, wt = 4%.

matrices. The highly porous and close slice-like structure can be clearly observed. The inherent layered structure was revealed by the lay-up of the MMT particles. By mapping the silicon distribution through EDX (Fig. 1(b) and (d)), the overall dispersion of clay particles in the polymeric matrix can be clearly observed. The introduced MMT particles, which are found homogenously dispersed in SA-MMT and PAM/SA-MMT nanocomposites, seems to loose the surface and generate many pleats.

The EDX spectra of SA-MMT and PAM/SA-MMT were depicted in Fig. 1(c) and (f). Eight elements were observed, i.e. C, O, Na, Mg, Al, Si, Pt, and Au. The C and O were due to the introduced organic modifier SA and intercalant AM. The N belonged to AM. The Na belonged to SA. The Pt and Au were associated with the coating materials sputtered on the sample. All the remaining elements represent the components of MMT. The carbon content based on the C/Si ratio in the PAM/SA-MMT was substantially higher than that of SA-MMT, which can be ascribed to some intercalation of MMT with PAM chains [36]. After the MMT incorporation into the polymeric network of PAM, the chemical environment of $–COO^-$ and –

CONH– of PAM has changed and exerted a positive influence on the absorbing ability of PAM/SA-MMT [33]. It can be concluded that MMT participated in the graft-polymerization of SA-MMT with AM and the formation of the intercalate-exfoliated nanostructure of PAM/SA-MMT, which improved the polymeric network and enhanced the adsorption capacity.

The XRD patterns of MMT and SA modified MMT are compared in Fig. 2. XRD analysis is a classical technique to accurately characterize the d (0 0 1) interlayer spacing of MMT [17]. A prominent peak corresponding to the 0 0 1 reflection of MMT occurred at 2θ of 8.81°. The average basal d spacing of 1.00 nm was calculated for this reflection using Bragg's equation:

$$2d \sin\theta = \lambda \quad (8)$$

The 0 0 1 peak could also be observed in the scattering curve of SA modified MMT, which remained in the same position and became much broader. The shift of 001 peak to smaller angles observed in modified MMT with polysaccharides such as chitosan normally indicates the intercalation of modifiers into the stacked MMT layers and the destruction of MMT crystalline structure [28]. However, the broadening XRD pattern of 0 0 1 peak observed in SA-modified MMT reflected a lower degree of ordering for MMT layers with original MMT, which led to the irregular arrangement of MMT layers [37]. No shift of 001 peak indicated that the reaction between SA and MMT occurred on the external surfaces of MMT particles, which verified their bonding interactions observed in FT-IR results.

The FT-IR spectra of MMT, SA, and SA-modified MMT are shown in Fig. 3(a). In the spectrum of SA-modified MMT, the –OH stretching vibration of silanol (Si–OH) group of MMT at 3,620 cm^{-1} shifted to higher wave number 3,625 cm^{-1} [38]. The peak 1,613 cm^{-1} of SA and the peak 1,634 cm^{-1} of MMT, which corresponded to the asymmetric stretching vibration of $–COO^-$ group and the bending vibration of H–OH bond, shifted to 1,626 cm^{-1} in SA-modified MMT, suggesting the bonding action between $–COO^-$ group of SA and –OH of MMT [17]. The stretching vibration of in-plane Si–O–Si bond of MMT at 1,048 cm^{-1} and the asymmetric C–O–C stretch of SA at 1,031 cm^{-1} were overlapped to 1,043 cm^{-1}, indicating their strong interaction [38]. The bending and deformation vibrations of the Si–O bond of MMT at 528 and 475 cm^{-1} also shifted to 524 and 469 cm^{-1} in SA-modified MMT [39].

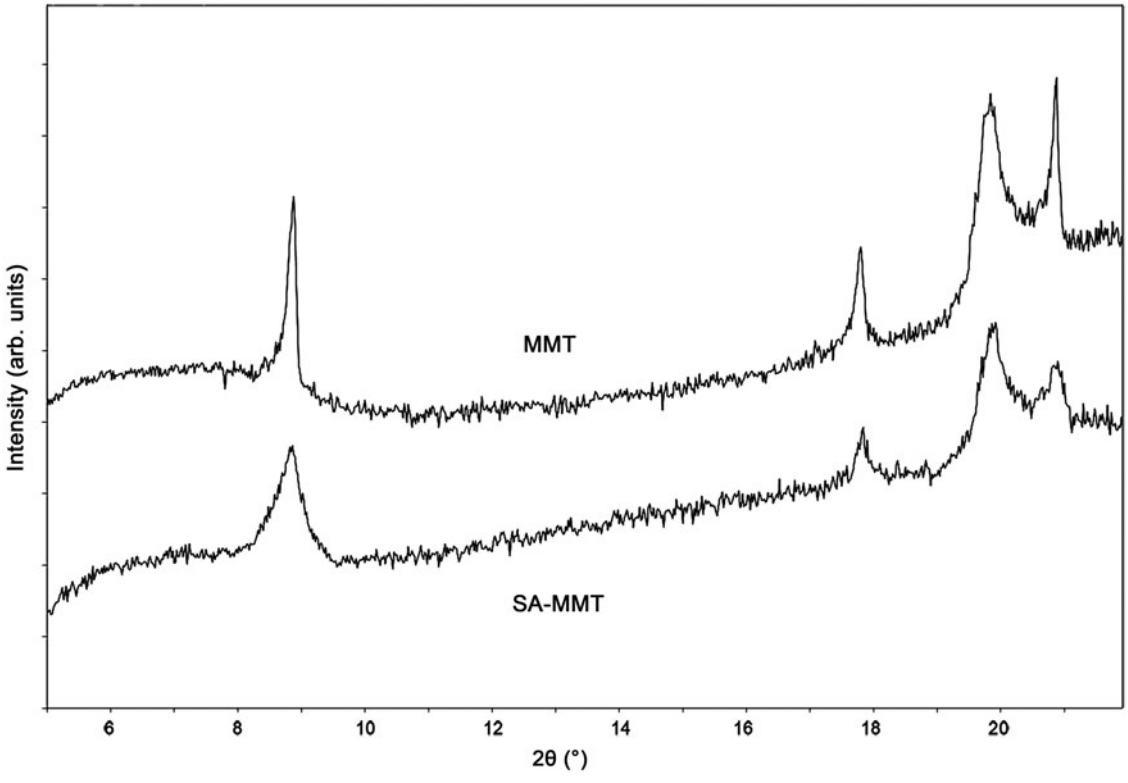

Fig. 2. XRD patterns of MMT and SA-modified MMT; wr = 60, wt = 4%.

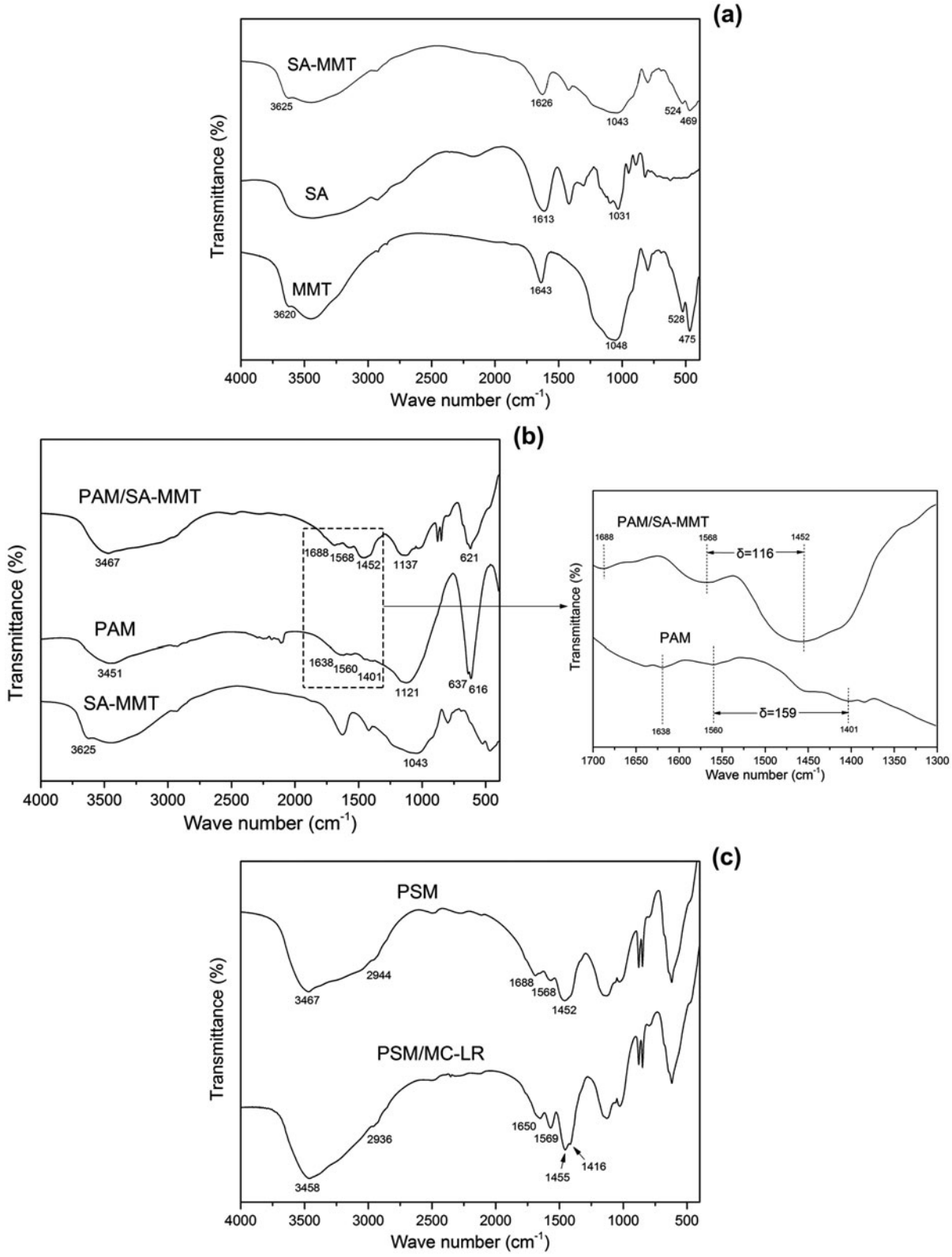

Fig. 3. FT-IR spectra of MMT, SA, and SA-modified MMT (a), SA-MMT, PAM, and PAM/SA-MMT (b), and PAM/SA-MMT before and after MC-LR adsorption (c); wr = 60, wt = 4%.

The FT-IR spectra of SA-modified MMT, PAM, and PAM/SA-MMT are shown in Fig. 3(b). The adsorption band ascribed to –OH stretching vibration of MMT at 3,625 cm^{-1} disappeared in the spectrum of PAM/SA-MMT, while the peak at 3,451 cm^{-1} of PAM chain shifted to 3,467 cm^{-1}. The PAM chains at 1,638 and 1,121 cm^{-1} shifted to 1,688 and 1,137 cm^{-1}, while the stretching vibration of Si–O–Si bond at 1,043 cm^{-1} disappeared. These results indicated the bonding actions between –OH and Si–O–Si of MMT and –CONH– of PAM chains [17]. The splitting δ between the asymmetric and symmetric $–COO^-$ vibration bands decreased from 159 to 116, suggesting that the physical cross-linking interactions originated between $–COO^-$ of PAM chains to MMT would increase in PAM/SA-MMT [17]. We could therefore deduce the schematic preparation process of PAM/SA-MMT superabsorbent nanocomposite in Fig. 4.

The FT-IR spectra of PAM/SA-MMT before and after sorption of MC-LR are shown in Fig. 3(c). According to the FT-IR spectrum, the –OH stretching mode of PAM/SA-MMT shifted from 3,467 to 3,458 cm^{-1}, characterizing the formation of hydrogen bonding between MC-LR and the –OH groups of MMT or SA. The movement of the methylene vibration band from 2,944 to 2,936 cm^{-1} indicated that the adsorption process might involve some hydrophobic interactions. The asymmetric $–COO^-$ vibration band at 1,571 cm^{-1} shifted to lower wave number 1,566 cm^{-1}; the symmetric $–COO^-$ vibration band at 1,436 cm^{-1} was split apart into 1,446 and 1,405 cm^{-1}. These two variations suggested the strong electrostatic interaction

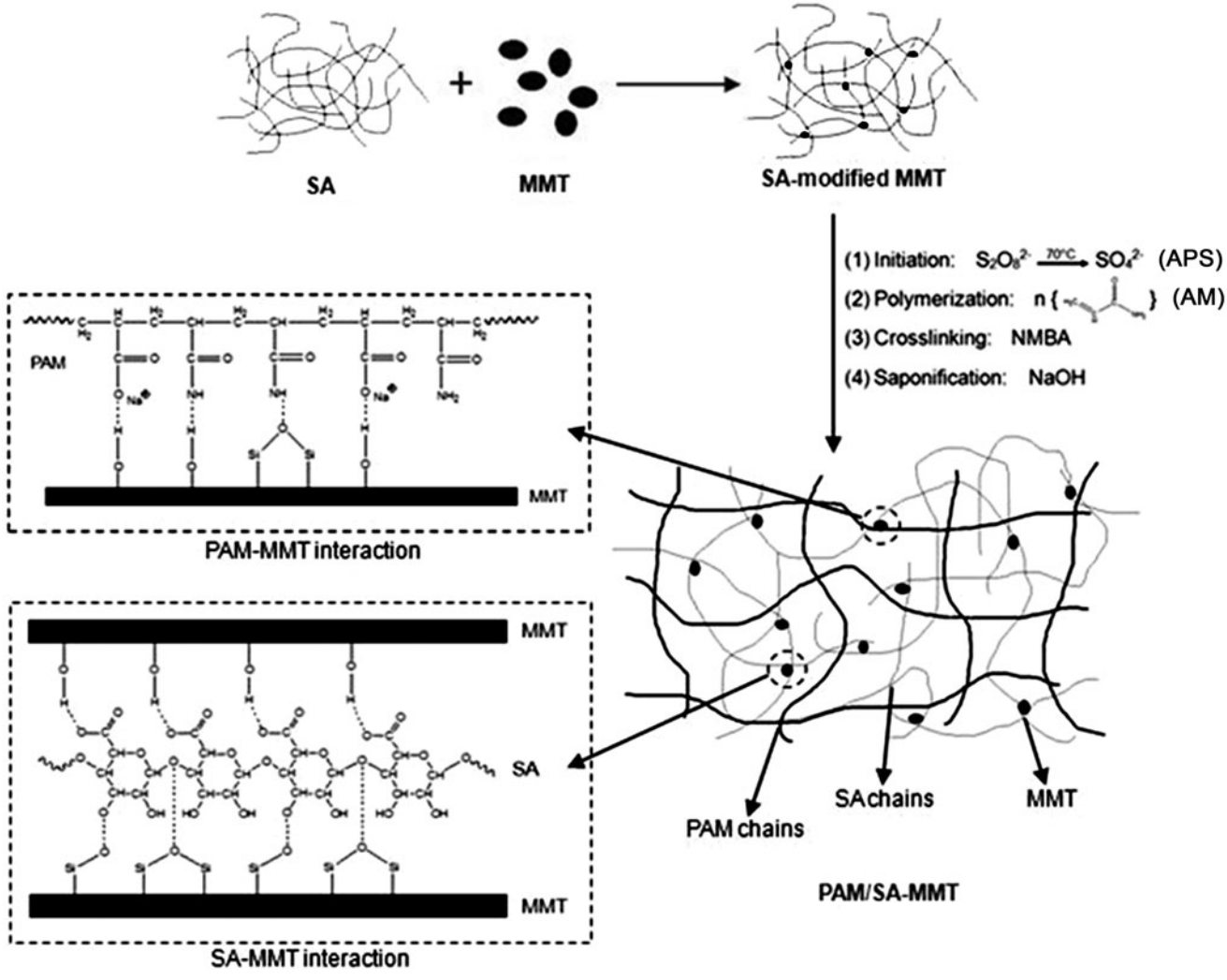

Fig. 4. Schematic preparation process of PAM/SA-MMT superabsorbent nanocomposite.

between MC-LR and the $-COO^-$ groups of PAM. The MC-LR adsorption process on PAM/SA-MMT could be presumed to involve the combining mechanism of hydrogen, hydrophobic, and electrostatic bonding.

3.2. RSM approach for MC-LR adsorption optimization

The Response surface model was established as an effective means of reflecting MC-LR adsorption process affected by the controlling parameters. The statistical significances of parameters and their interactions (combinations of two codes) at various levels of probability values are shown in Table 2, which are based on Student's *t*-test and *p*-values. A small *p*-value indicates a statistically significant parameter effect [40], and a term with $p < 0.01$ was considered significant in this study. The *t*-value represents the ratio of the estimated parameter effect to the estimated parameter standard error. A large magnitude of *t*-value represents the statistical significance of the corresponding variable in the regression model [41]. High values of the parameter estimates for these variables with high levels of significance indicated their importance in the sorption process. The selected first-order (A, B, C), second-order (A^2, B^2, C^2), and interactive parameters (BC) were shown to be statistically significant except for the interaction effect of pH—wr AM/SA (AB) and pH—wt MMT (AC). The linear term of wt% MMT was found as the most significant component of the regression model (estimated coefficient = −27.55, $t = -14.06$, $F = 198.42$, $p < 0.01$) for the present application. The pH effect was also highly significant (estimated coefficient = −23.56, $t = -12.02$, $F = 145.14$, $p < 0.01$). Only wr AM/SA showed a significant positive relationship with adsorption, while all other variables had negative effects on the adsorption process.

By fitting the parameter coefficients estimated by RSM based on Box–Behnken design (Table 2) and emphasizing the most significant polynomial terms, the final second-order regression equation in terms of coded factors to describe MC-LR adsorption by PAM/SA-MMT was

$$Y = 455.40 - 23.56A + 12.94B - 27.55C - 8.45AB - 3.23AC - 12.08BC - 13.83A^2 - 28.58B^2 - 13.60C^2 \quad (9)$$

The coded response values of the independent variables were entered into the established design to fit the suggested numerical model. By plotting the predicted responses according to the final quadratic polynomial equation, we could then obtain the rotatable 3D response surface plots and explain the regular pattern of experimental data variances.

The experimental data were subjected to the analysis of variance (ANOVA) to test the accuracy and applicability of the Response surface model. The ANOVA results in Table 3 show that the MC-LR adsorption regression model was significant, because of the low probability value of p (<0.01) and the high Fisher *F*-test value (66.34), which means that there is only 0.01% chance that a model *F*-value this large could occur because of noise. The pure error of zero indicates that the lack of fit was not significant. The goodness of regression was also verified by the low coefficient of variation (C.V.) and the high coefficients of R^2, which indicates the high dependence between the observed and the simulated response values. The precision was evaluated by the signal-to-noise ratio, which compares the range of predicted values at the design points to the average prediction error. Its

Table 2
Estimated coded parameters of the Box–Behnken model of MC-LR adsorption by PAM/SA-MMT and their statistical significance

Variables	Parameter coefficient	Mean square	Standard error	*t*-value	*F*-value	*p*-value > *F*
Intercept	455.40					
A	−23.56	4441.53	1.96	−12.02	145.14	<0.01
B	12.94	1339.03	1.96	6.60	43.76	<0.01
C	−27.55	6072.02	1.96	−14.06	198.42	<0.01
AB	−8.45	285.61	2.77	−3.05	9.33	0.02*
AC	−3.23	41.60	2.77	−1.17	1.36	0.28*
BC	−12.08	583.22	2.77	−4.36	19.06	<0.01
A^2	−13.83	804.76	2.70	−5.12	26.30	<0.01
B^2	−28.58	3438.02	2.70	−10.59	112.34	<0.01
C^2	−13.60	778.78	2.70	−5.04	25.45	<0.01

*$p > 0.01$, non-significant parameter.

Table 3
ANOVA for Box–Behnken response surface model of MC-LR adsorption by PAM/SA-MMT

Sources of variation	Sum of squares	Degree of Freedom	Mean square	*F*-value	*p*-value > *F*
Model	18271.38	9	2030.15	66.34	<0.01
Residual	214.22	7	30.60		
−Lack of fit	214.22	3	71.41		
−Pure error	0	4	0		
RMSE	5.53	R^2		0.9884	
Mean	429.05	Adjusted R^2		0.9735	
C.V.* (%)	1.29	Predicted R^2		0.8146	
		Adequate precision		24.09	

*C.V. = RMSE/mean.

relatively high value (24.09) indicates a satisfactory model for discrimination and an authentic relationship between the model responses and significant variables. The model adequacy could be checked by all information on the lack of fit contained in the residuals [42]. The normal probability plot of residuals (Fig. 5) is a graphical diagnostic tool, which confirms the assumptions that errors are normally distributed and error variances are homogeneous. No serious deviation between observed and predicted values is indicated. Thus, this regression model can be used to navigate the design space and analyze the response patterns for optimization.

3.3. Interactive effects of variables on MC-LR adsorption capacity of PAM/SA-MMT

3D response surface plots were investigated to predict the variations of MC-LR removal capacity under different controlling parameters. The interactive effects of pH, wr of PAM to SA, and wt of MMT on MC-LR adsorption by PAM/SA-MMT is respectively depicted in Fig. 6. Graphical optimization of the response surface plots with DX analysis was also performed to determine the range of the optimal pH condition and the feed composition of superabsorbent that maximizes the removal percentage of MC-LR.

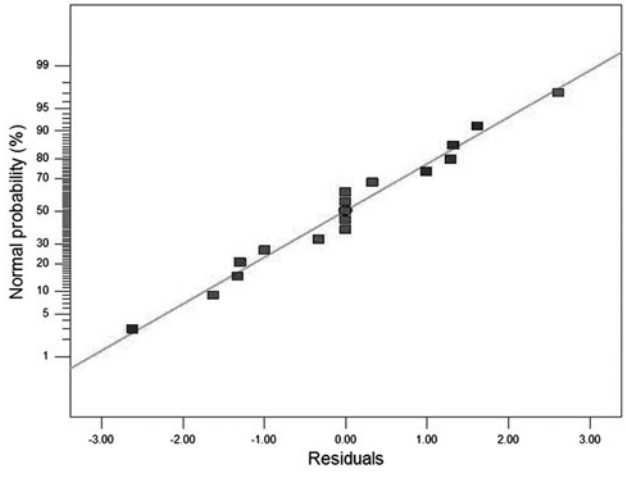

Fig. 5. Normal probability plot of residuals.

The optimal pH was found between 2.5 and 4.5, and at higher or lower pH the adsorption capacity of PAM/SA-MMT for MC-LR was less. The adsorption initially increased and then decreased slightly with increasing wr from 20 to 80. Similarly, decreasing wt from 20 to 5% facilitated the removal of MC-LR, but markedly restrain the adsorption with wt from 3 to 1%. The maximum adsorption was observed with pH 2.5–4.5, wr AM/SA 55–65 and wt MMT 3–5%.

The modeling results could be interpreted as follows: more PAM molecules could be provided next to the chains to propagate sites of SA with increasing wr, which enhances the amounts of –COOH groups and ameliorate the adsorption capacity; plus, more Na^+ generated in the poly-network during the neutralization process of PAM would enhance the osmotic pressure difference between superabsorbent and adsorbate, which also improve the MC-LR uptake [12]. The introduced nano-sized MMT K-10 generated a loose and porous surface for PAM/SA-MMT, and the expanded PAM/SA-MMT surface favored the interaction between MC-LR molecules and vacant adsorption sites of the larger adsorbent surface [17]. The broad surface also benefited the penetration of MC-LR molecule into the poly-network. However, with MMT content increasing, the poly-network of PAM/SA-MMT became intensive and formed more cross links, which might suppress the elasticity of polymer chains.

The solution chemistry significantly affects the MC-LR adsorption process [43]. The response of the overall charges on MC-LR and PAM/SA-MMT to

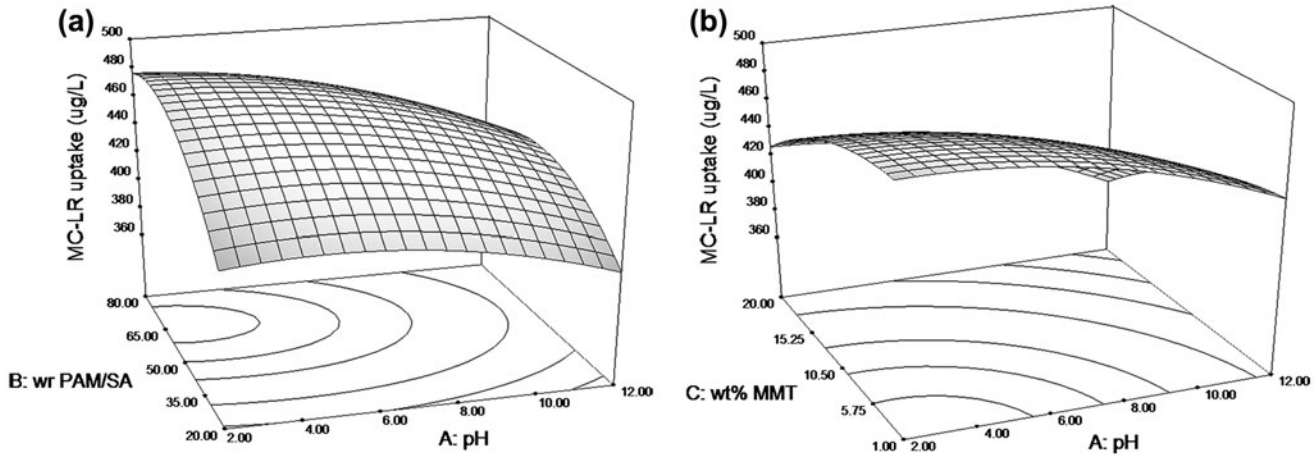

Fig. 6. 3D Box–Behnken response surface plots of MC-LR uptake by PAM/SA-MMT as a function of pH—wr of PAM to SA (a) and pH—wt of MMT (b).

changes in pH significantly affects the performance of their surface ionizable groups. The pH_{pzc} of PAM/SA-MMT was found to be 6.2, and PAM/SA-MMT had cationic surface charges at pH < 6.2 and anionic surface charges at pH > 6.2. Otherwise, the MC-LR molecule remained neutral in the narrow pH range of 2.09–2.19, producing cationic species $[(COOH)_2(NH_2^+)]$ at pH < 2.09 and anionic species $[(COO^-)_2(NH_2^+)$ and $(COO^-)_2(NH)]$ at pH > 2.19 [44]. The physical ion pairing effect indicates that the increase in ionic interaction, leads to better adsorption, which can be observed when MC-LR and PAM/SA-MMT carry opposite surface charges.

In our study, the maximum MC-LR adsorption capacity of PAM/SA-MMT was observed between pH 2.5–4.5, which can be mainly attributed to the electrostatic attraction, while MC-LR was essentially in an anionic form and PAM/SA-MMT was in a cationic form at this pH. As the system pH increased, the cationic surface charges of PAM/SA-MMT decreased to pH_{pzc} (6.2), and then the –COOH group of PAM/SA-MMT present in acrylate dissociated to form increasing anionic $–COO^-$, which repelled the same charge carried by MC-LR. Below pH 2.5, both adsorbent and adsorbate had increasing cationic surface charges, and the repulsion between positive charges caused a decrease in adsorption for MC-LR. Further investigations should be undertaken to evaluate whether the strong surface complexation reactions were involved in the pH range of pH_{pzc}.

Furthermore, the MC-LR molecular shape is pH dependent [43]. MC-LR tends to remain in aqueous phase rather than being adsorbed to PAM/SA-MMT with increasing pH owing to the partitioning effect of the charged MC-LR molecule [35]. Conversely, a decrease of MC-LR water solubility and a higher MC-LR affinity for PAM/SA-MMT surface at lower pH were expected. MC-LR behaves as a polyelectrolyte in solution, and the overall molecular dimension decreases with the stronger intramolecular forces at low pH, increasing the possibility of adsorption [11].

To confirm the validity of our statistical and experimental strategies, we performed a series of experimental tests in three replicates, and the results indicated that the maximum MC-LR removal (479.37 $\pm$ 1.23 $\mu g\,L^{-1}$) was obtained with all the parameters at the optimum values (pH = 3.5, wr = 60, wt = 4%). The confirmatory experiments demonstrated that the model prediction (481.32 $\mu g\,L^{-1}$) was in good accordance with the experimental result. The modeling optimization of the adsorption process affected by interactive variables is consistent with our experimental observations.

3.4. Effects of pH and temperature on MC-LR removal

Variations of adsorption capacities of samples (wr = 60, wt = 4%) with different pH and temperature were studied by performing a batch of equilibrium experiments and shown in Fig. 7. With increase in pH, the equilibrium of MC-LR removal capacity of PAM/SA-MMT rapidly increased before reaching a peak of 9.16–9.52 $mg\,g^{-1}$ at the range of pH 2.5–5.0, and then continuously decreased to 8.34–8.54 $mg\,g^{-1}$ at pH 12 (alkaline environment). The MC-LR adsorption capacity of PAM/SA-MMT increased with increase in temperature from 10 to 40 ℃.

The analogy to explain the pH effect is the physical ion pairing effect and the partitioning effect of charged MC-LR molecules in the aqueous phase, as

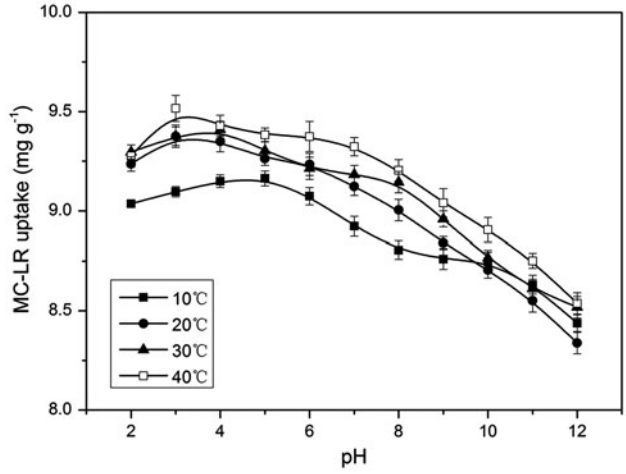

Fig. 7. Effects of pH and temperature on the MC-LR adsorption onto PAM/SA-MMT (wr = 60, wt = 4%).

previously demonstrated. The temperature study becomes necessary to understand the influence of changing temperature in the real environment due to seasonal variations. The observations indicated the possibility about the endothermic behavior of the adsorption process in the range of 10–40℃. High temperature would possibly enhance the diffusion rate of adsorbate ions and allow the breaking and formation of bonds on adsorbent surface. Increasing temperature would also produce a swelling effect within the internal structure of adsorbent, penetrating further the toxin molecules [12].

3.5. Kinetic modeling: effects of initial MC-LR concentration and contact time

The variation of MC-LR uptake amount with different initial MC-LR concentrations vs. contact time is shown in Fig. 8(a). As the MC-LR adsorption capacity of PAM/SA-MMT reached a maximum around pH 3.5, kinetic experiments were conducted for different time intervals at pH 3.5 and ambient temperature. With initial MC-LR concentrations ranging from 100 to 500 μg L^{-1}, the MC-LR removal percentage at equilibrium decreased from 96.3 to 93.7%. The adsorption equilibrium was achieved within 80 min for the initial MC-LR concentration of 100–200 μg L^{-1}, whereas the equilibrium time was longer (over 90 min) for higher initial concentrations.

The removal efficiency appeared to be dependent on MC-LR initial concentration with fixed adsorbent dosage. The decrease of MC-LR uptake at high MC-LR concentration can be explained by increased competition between MC ions for an unchangeable number of available binding sites and also saturation

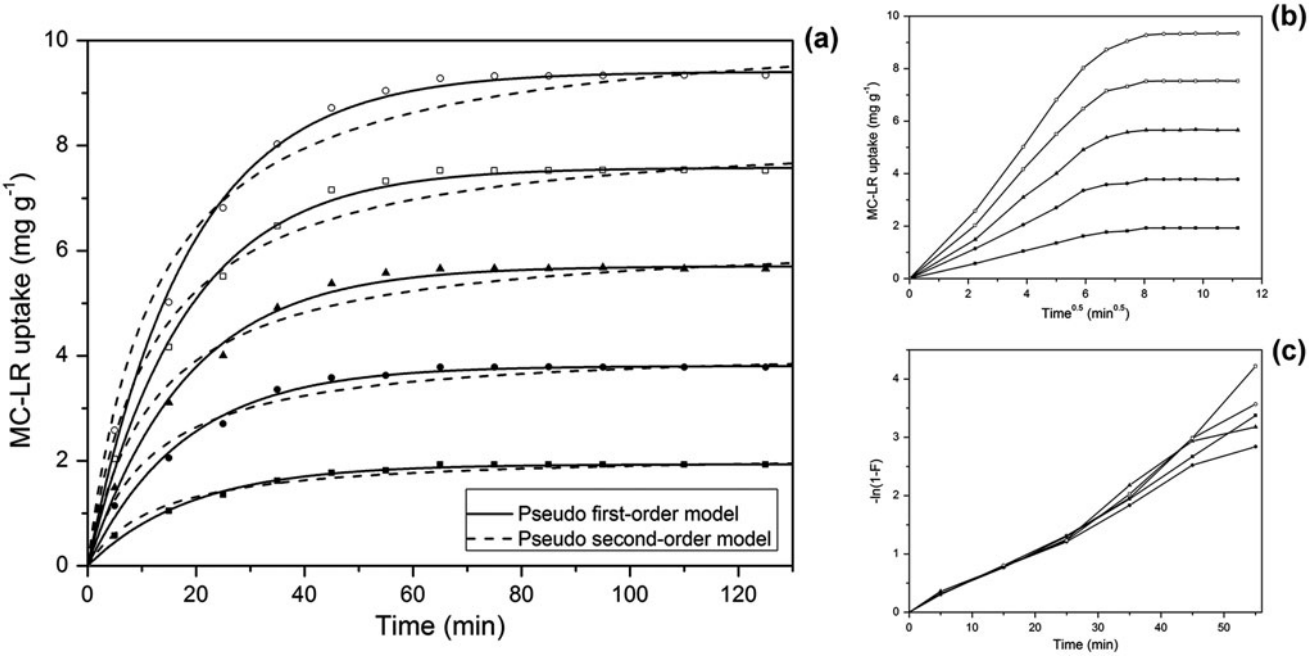

Fig. 8. Kinetic plots (a), intraparticle diffusion plots (b), and liquid film diffusion plots (c) for MC-LR adsorption to PAM/SA-MMT with initial concentrations of 100 μg L^{-1} (black square), 200 μg L^{-1} (black circle), 300 μg L^{-1} (black triangle), 400 μg L^{-1} (white square), and 500 μg L^{-1} (white circle).

of most binding sites. The aggregation of MC-LR molecules might prevent them from diffusing deeper in the nanocomposite structure of PAM/SA-MMT. Compared with the amount of MC-LR, the available surface area decreased with higher initial concentrations and led to longer equilibrium times. The short equilibrium time of PAM/SA-MMT for MC-LR removal indicates that it is a much more efficient adsorbent than other reported absorbents [90 min for peat [35], 200 min for chitosan–cellulose composite material [45], 8 h for carbon nanotube [6], 16 h for activated carbon from coal [11], 24 h for nanosilicate platelet [46], 24 h for sediments [47,48]], suggesting its potential use for large-scale industrial application.

The experimental kinetic data were fitted to the pseudo-first-order and pseudo-second-order models. The non-linear forms of these two models are

$$Q_t = Q_e(1 - \exp(-k_1 t)) \tag{10}$$

$$Q_t = \frac{{Q_e}^2 k_2 t}{1 + Q_e k_2 t} \tag{11}$$

where Q_t is the amount of MC-LR adsorbed at time t (mg g^{-1}), Q_e is the amount of MC-LR uptake at equilibrium (mg g^{-1}), k_1 is the pseudo-first-order equilibrium rate constant (min^{-1}), and k_2 is the pseudo-second-order equilibrium rate constant (g mg^{-1} min^{-1}).

The reduced chi-squared test and the adjusted R^2 were defined as a statistical measure of the goodness of fit

$${\chi_{red}}^2 = \sum_{i=1}^{n} \frac{(Q_i - q_i)^2}{(n-2)q_i} \tag{12}$$

$${R_{adj}}^2 = \frac{(n-1)R^2 - 1}{n-2} \tag{13}$$

A small ${\chi_{red}}^2$ and a high ${R_{adj}}^2$ indicate good curve fitting and similarity between the experimental data and model. The parameters of both kinetic models and the ${\chi_{red}}^2$ and ${R_{adj}}^2$ values are shown in Table 4. The amount of adsorbed MC-LR at equilibrium (Q_e) and the rate constants (k) were calculated from the slopes and intercepts of these curves. Both pseudo models slightly overestimated the removal before 25 min and underestimated the removal after 25 min till equilibrium, but they were still consistent with the experimental data in general, especially at low concentrations. A reasonable explanation is that the rate-controlling step should not be sole and the sorption process involves both physical and chemical interactions. The pseudo-first-order model fit well most kinetic data for the whole range of contact time and underestimate the Q_e values [35]. The pseudo-second-order model fits much better with the chemisorption rate-controlling process [49]. The underestimation was possibly because a weak external resistance delayed the initiation of the sorption process, which decreases the validity of the simulations.

The high initial adsorption rate was observed and the plateau of the final equilibrium was shortly reached thereafter. The availability of numerous vacant sites and easy diffusion into the particle pores led to the initial rapid uptake. The decreasing trend of initial average sorption rate indicates the existence of strong attractive forces and the probability of fast intraparticle diffusion [50]. An increased concentration gradient between adsorbed and remaining MC-LR could be observed and explained by the gradual filling-up and regeneration process of a large number of available sorption surface sites [51].

The sorption process before reaching equilibrium can be defined by three steps: (1) transfer of the adsorbate from the solution to the boundary liquid film and onto the surface of the sorbent particle (film diffusion), (2) transfer of the adsorbate from the sorbent surface into the intraparticle active binding sites (particle diffusion), and (3) interaction between the adsorbates and the active binding sites [52]. The liquid film

Table 4
Kinetic parameters for MC-LR adsorption onto PAM/SA-MMT

MC-LR initial concentration (μg L^{-1})	Q_e (exp) (mg g^{-1})	Pseudo-first-order kinetic model			Pseudo-second-order kinetic model		
		Q_e (cal) (mg g^{-1})	${\chi_{red}}^2$	${R_{adj}}^2$	Q_e (cal) (mg g^{-1})	${\chi_{red}}^2$	${R_{adj}}^2$
100	1.93	1.94	0.0015	0.9950	2.14	0.0058	0.9813
200	3.78	3.81	0.0069	0.9942	4.19	0.0285	0.9759
300	5.66	5.71	0.0102	0.9963	6.31	0.0737	0.9731
400	7.53	7.58	0.0109	0.9977	8.37	0.1109	0.9768
500	9.37	9.41	0.0167	0.9977	10.41	0.1545	0.9790

diffusion model [53] and the intraparticle diffusion model [54] were defined as

$$-\ln(1 - Q_t/Q_e) = k_{fd}t \quad (14)$$

$$Q_t = k_{id}t^{0.5} \quad (15)$$

where Q_t is the amount of MC-LR adsorbed at time t (mg g^{-1}), Q_e is the amount of MC-LR uptake at equilibrium (mg g^{-1}), k_{id} is the intraparticle diffusion constant (mg g^{-1} min^{-1}), and k_{fd} is the film diffusion rate constant (min^{-1}).

The third step of the bonding interaction is normally considered to be very rapid. These two models are used to clarify the mechanism involved in the first two steps of the sorption process, as shown in Fig. 8(b) and (c). Intraparticle diffusion or film diffusion may be the main mechanism for the kinetics only if its model plot is a straight line passing through the origin [52]. The calculated values of the intraparticle diffusion constant k_{id} were 0.23, 0.46, 0.71, 0.93, and 1.15 g mg^{-1} min^{-1} with nonzero intercepts for different initial MC-LR concentrations. The multi-linearity could be clearly observed from the plot of Q_t vs. $t^{0.5}$ curves, suggesting that the sorption process involved more than one kinetic stage and intraparticle diffusion might not be the only rate-controlling step. The plots of $-\ln(1-Q_t/Q_e)$ vs. t before 25 min are shown according to the liquid film diffusion model, and all depict a straight line with a near-zero intercept and a slope (k_{fd}) of 0.049. We can conclude that the MC-LR sorption process begins with the fastest liquid film diffusion phase over the adsorbent surface with a considerable contribution from intraparticle diffusion. The second phase can be attributed to relatively fast intraparticle diffusion followed by the third stage of micropore diffusion before the equilibrium. Neither intraparticle diffusion nor film diffusion is considered as the sole rate-controlling mechanism of MC-LR adsorption to PAM/SA-MMT.

3.6. Sorption isotherm modeling

The isotherms determined at different initial MC-LR concentrations ranging from 100 to 1,000 μg L^{-1} at pH 3.5 and ambient temperature were studied to describe the sorption of MC-LR to PAM/SA-MMT (Fig. 9). The Γ-shaped sorption isotherm plot described a decreasing ratio of MC-LR concentration remaining in solution to MC-LR adsorbed to PAM/SA-MMT with increasing initial adsorbate concentration, providing a concave curve without plateau. Langmuir and Freundlich models were applied to the isotherm to empirically predict

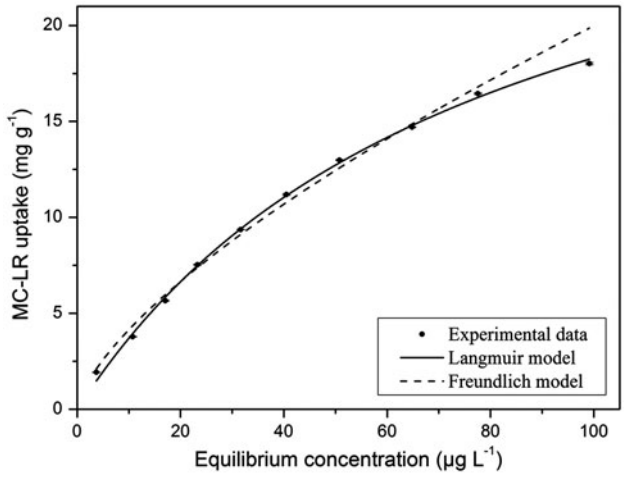

Fig. 9. MC-LR sorption isotherm of PAM/SA-MMT at pH 3.5.

the extent of adsorption process and interpret the nonlinear equilibrium relationship between adsorbed and remaining MC-LR. The favorable adjusted R^2 and reduced chi-squared values revealed the validity of both simulation models (Table 5). The equations of Langmuir and Freundlich models are

$$Q = \frac{Q_{max}b_L C_{eq}}{1 + b_L C_{eq}} \quad (16)$$

$$Q = k_F\ C_f^{1/n} \quad (17)$$

where Q is the amount of MC-LR uptake by PAM/SA-MMT at equilibrium (mg g^{-1}), C_{eq} is the amount of MC-LR remaining in solution at equilibrium (μg L^{-1}), Q_{max} is the maximum MC-LR uptake by PAM/SA-MMT (mg g^{-1}), b_L is the Langmuir equilibrium constant (L μg^{-1}), k_F is the Freundlich equilibrium

Table 5
Langmuir and Freundlich isotherm constants for MC-LR adsorption onto PAM/SA-MMT

Q_{max} (mg g^{-1})	b_L (L μg^{-1})	R_{adj}^2	χ_{red}^2
Langmuir model			
32.66	0.013	0.9973	144.61
k_F (g^{-1})	n	R_{adj}^2	χ_{red}^2
Freundlich model			
0.86	1.46	0.9915	447.27

constant (L mg^{-1}), and n is the dependence degree of the sorption equilibrium.

The Langmuir model showed a better fit to the experimental results than Freundlich model, which confirmed the assumptions that adsorption sites are identical, the sorption process is monolayer, and the adsorbent surfaces are homogeneous, [55]. Freundlich model describes better the sorption at low and intermediate concentrations on heterogeneous adsorbent surfaces or surfaces having adsorption sites with different affinities [35]. The process of MC-LR adsorption onto PAM/SA-MMT could therefore be characterized as the monolayer coverage of MC-LR molecule on the homogeneous surface of the nanocomposite. Plus, the adsorption sites have uniform energies and the interactions between the adsorbed MC-LR molecules are negligible. The specific surface and sorption capacity of PAM/SA-MMT was limited, as described by the Langmuir isotherm, rather than the exponentially increasing sorption process assumed by the Freundlich model.

The theoretical maximum MC-LR adsorption capacity of PAM/SA-MMT (32.66 mg g^{-1}) estimated by the Langmuir model is favorably comparable to most low-cost adsorbents reported in the literature as shown in Table 6. The outstanding adsorption capacity of PAM/SA-MMT indicates its feasibility as an efficient MC-LR remover from aqueous solutions. In addition, the high value of the Langmuir constant b_L indicates a steep initial slope of the isotherm, representing desirably high sorption energy and high affinity between the adsorbent and adsorbate. Similarly, the high values of the Freundlich constants k_F and $1/n$ indicate the high binding capacity between MC-LR and PAM/SA-MMT.

The economical comparison of PAM/SA-MMT superabsorbent nanocomposite with other adsorbents was also performed. The material prices for the comparison were obtained from the most recent information source published by the main international manufacturer or supplier of industrial raw materials. The average price of C18 silica and powder activated carbon from Acros® is $400 and $7.5 per 100 g, respectively. The average price of HP20 resin from Alibaba® is $12.6 per 100 g. The price of multi-walled carbon nanotubes from Alibaba® and Sigma–Aldrich® varies from $125 to $2000 per 100 g. The average cost of production of PAM/SA-MMT superabsorbent nanocomposite was $4.9 per 100 g, which is significantly lower than the aforementioned common adsorbents.

Table 6
Comparison of recent reported adsorption capacities of MC-LR on various adsorbents

Adsorbents	Q_{max} (mg g^{-1})	References
PAM/SA-MMT superabsorbent nanocomposite	32.66	Our data in the paper
Peat	0.23	[35]
Powdered activated carbon	0.75	[56]
Magnetic core mesoporous shell	20.00	[57]
HP20 resin	3.33	[58]
Graphene oxide	1.70	[8]
Ordered mesoporous silica	5.99	[59]

3.7. Regeneration cycling study in simulated ionic environment

The PAM/SA-MMT nanocomposite containing MMT could be regenerated, because its mechanical properties and physical form are protected by intercalated clays while pure hydrogels usually dissipate in aqueous phase [60]. To evaluate the reusability and cost-effectiveness of PAM/SA-MMT as an adsorbent, its performance through simulated adsorption/desorption cycles should be examined [8]. Desorption studies were first conducted in different media to evaluate the recovery of the adsorbate from the adsorbent and to select the appropriate desorbent. The highest desorption efficiency was observed in 0.1 M NaOH (92.1%), since MC-LR showed increasing hydrophilicity and had a tendency to remain in the aqueous phase with increasing pH. Only physisorbed MC-LR molecules

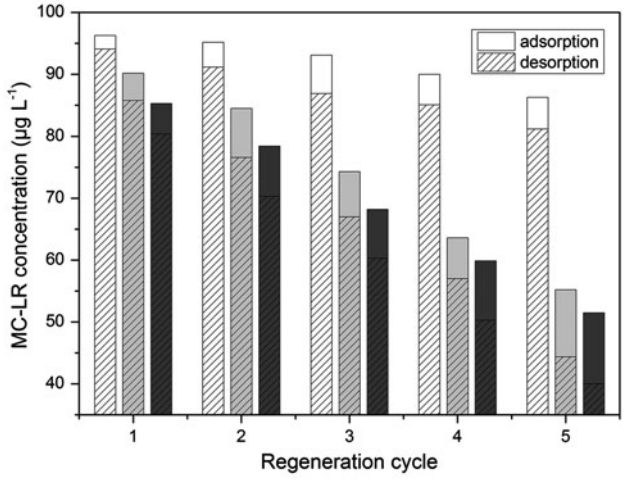

Fig. 10. Adsorption/desorption cycles of MC-LR with concentrations of ions for simulation of 0 (white), 25 (gray), and 50 mg L^{-1} (black).

can be desorbed from the surface of the adsorbent, the pH effect on adsorption and desorption highlighted the strong binding reaction, and revealed the possibility of chemisorption mechanisms involved in the MC-LR removal [51].

The regeneration capacity decreased faster in counter ionic environment. As shown in Fig. 10, MC-LR removals in the presence of cations and anions decreased from 90.2 to 55.2% and from 85.3 to 51.5% during the five regeneration cycles, respectively, while the concentration of counter ions ranged between 25 and 50 mg/L. The concentration of counter ions showed a major effect on the adsorption efficiency. In theory, the increasing ionic strength leads to the decrease of adsorption capacity where the electrostatic attraction between PAM/SA-MMT surface and MC-LR ions is hindered [8]. The transfer of MC-LR molecules from aqueous phase to solid phase is found significantly affected by counter ions in this study.

The first five cycles without excess ionic effect resulted in over 85% adsorption and 80% desorption. The decrease of adsorption efficiency in regeneration cycles can be attributed to the loss of surface functional charge groups [8]. However, the recovery of MC-LR after each desorption cycle reached 92.8%, which is advantageous for numerous cycles and the disposal of spent superabsorbents.

4. Conclusions

In the present study, the process of PAM/SA-MMT preparation and MC-LR adsorption was characterized by SEM, EDX microanalysis, XRD analysis, and FT-IR analysis. The empirical relationship between its MC-LR adsorption capacity and the independent controlling parameters was investigated based on the RSM approach. The interactive effects of pH, wr of AM to SA, and wt of MMT on MC-LR removal were optimized by using the Box–Behnken experimental design and fitting the quadratic statistical model. The maximum adsorption capacity was observed with pH 2.5–4.5, wr 55–65, and wt 3–5%. The MC-LR adsorption capacity of PAM/SA-MMT increased with increasing temperature from 10 to 40˚C. The equilibrium time of the sorption process was shown to be 80 min through kinetic analysis and pseudo models revealed that several different rate-controlling kinetic stages were involved. The Langmuir isotherm model predicted that the theoretical maximum adsorption capacity of PAM/SA-MMT was 32.66 mg g^{-1}. PAM/SA-MMT is found effective, environmentally benign, and economically accessible for regenerative cycling. The laboratory-scale module thus provided a valuable option for PAM/SA-MMT superabsorbent nanocomposite to become a potential adsorbent for large-scale applications on MC-LR removal.

Acknowledgment

We are grateful to all anonymous editors and reviewers for providing comments on this manuscript. We also appreciate the generous financial support of this work provided by the National Science Fund for Creative Research Groups of China (No. 51421006), the National Science Fund for Distinguished Young Scholars (No. 51225901), the Program for Changjiang Scholars and Innovative Research Team in University (No. IRT13061), the Outstanding Youth Fund of Jiangsu Province (No. BK2012037), the Fundamental Research Fund for the Central Universities (No. 2014B03814), and PAPD.

References

[1] J. Pietsch, K. Bornmann, W. Schmidt, Relevance of intra- and extracellular cyanotoxins for drinking water treatment, Acta Hydroch. Hydrob. 30 (2002) 7–15.
[2] J.H. Landsberg, The effects of harmful algal blooms on aquatic organisms, Rev. Fish. Sci. 10 (2002) 113–390.
[3] D.R. de Figueiredo, U.M. Azeiteiro, S.M. Esteves, F.J. Gonçalves, M.J. Pereira, Microcystin-producing blooms—A serious global public health issue, Ecotoxicol. Environ. Saf. 59 (2004) 151–163.
[4] A. Campos, V. Vasconcelos, Molecular mechanisms of microcystin toxicity in animal cells, Int. J. Mol. Sci. 11 (2010) 268–287.
[5] M. Thirumavalavan, Y.L. Hu, J.F. Lee, Effects of humic acid and suspended soils on adsorption and photodegradation of microcystin-LR onto samples from Taiwan reservoirs and rivers, J. Hazard. Mater. 217–218 (2012) 323–329.
[6] H. Yan, A. Gong, H. He, J. Zhou, Y. Wei, L. Lv, Adsorption of microcystins by carbon nanotubes, Chemosphere 62 (2006) 142–148.
[7] W. Chen, L. Song, L. Peng, N. Wan, X. Zhang, N. Gan, Reduction in microcystin concentrations in large and shallow lakes: Water and sediment-interface contributions, Water Res. 42 (2008) 763–773.
[8] S. Pavagadhi, A.L.L. Tang, M. Sathishkumar, K.P. Loh, R. Balasubramanian, Removal of microcystin-LR and microcystin-RR by graphene oxide: Adsorption and kinetic experiments, Water Res. 47 (2013) 4621–4629.
[9] R.J. Morris, D.E. Williams, H.A. Luu, C.F. Holmes, R.J. Andersen, S.E. Calvert, The adsorption of microcystin-LR by natural clay particles, Toxicon 38 (2000) 303–308.
[10] T. Munusamy, Y.L. Hu, J.F. Lee, Adsorption and photodegradation of microcystin-LR onto sediments collected from reservoirs and rivers in Taiwan: A laboratory study to investigate the fate, transfer, and degradation of microcystin-LR, Environ. Sci. Pollut. Res. 19 (2012) 2390–2399.
[11] W.J. Huang, B.L. Cheng, Y.L. Cheng, Adsorption of microcystin-*LR* by three types of activated carbon, J. Hazard. Mater. 141 (2007) 115–122.

[12] L. Wang, J. Zhang, A. Wang, Removal of methylene blue from aqueous solution using chitosan-*g*-poly (acrylic acid)/montmorillonite superadsorbent nanocomposite, Colloids Surf., A 322 (2008) 47–53.
[13] K. Kabiri, H. Omidian, M. Zohuriaan-Mehr, S. Doroudiani, Superabsorbent hydrogel composites and nanocomposites: A review. Polym. Compos. 32 (2011) 277–289.
[14] T. Singh, R. Singhal, Methyl Orange adsorption by reuse of a waste adsorbent poly (AAc/AM/SH)-MB superabsorbent hydrogel: Matrix effects, adsorption thermodynamic and kinetics studies, Desalin. Water Treat., ahead-of-print (2013) 1–15.
[15] Y.T. Xie, A.Q. Wang, Study on superabsorbent composites XIX. Synthesis, characterization and performance of chitosan-*g*-poly (acrylic acid)/vermiculite superabsorbent composites, J. Polym. Res. 16 (2009) 143–150.
[16] C. Nakason, T. Wohmang, A. Kaesaman, S. Kiatkamjornwong, Preparation of cassava starch-graft-polyacrylamide superabsorbents and associated composites by reactive blending, Carbohydr. Polym. 81 (2010) 348–357.
[17] H. Qiu, Z. Qiu, J. Wang, R. Zhang, F. Zheng, Enhanced swelling and methylene blue adsorption of polyacrylamide-based superabsorbents using alginate modified montmorillonite, J. Appl. Polym. Sci., 131(6) (2014) 1–9 (Article ID 40013).
[18] S. Wong, T. Teng, A. Ahmad, A. Zuhairi, G. Najafpour, Treatment of pulp and paper mill wastewater by polyacrylamide (PAM) in polymer induced flocculation, J. Hazard. Mater. 135 (2006) 378–388.
[19] A. Li, A. Wang, Synthesis and properties of clay-based superabsorbent composite, Eur. Polym. J. 41 (2005) 1630–1637.
[20] G. Crini, Recent developments in polysaccharide-based materials used as adsorbents in wastewater treatment, Prog. Polym. Sci. 30 (2005) 38–70.
[21] A. Esfandiari, H. Nazokdast, A.S. Rashidi, M.E. Yazdanshenas, Review of polymer-organoclay nanocomposites, J. Appl. Sci. 8 (2008) 545–561.
[22] Y. Li, X. Li, L. Zhou, X. Zhu, B. Li, Study on the synthesis and application of salt-resisting polymeric hydrogels, Polym. Adv. Technol. 15 (2004) 34–38.
[23] R. Srinivasan, Advances in application of natural clay and its composites in removal of biological, organic, and inorganic contaminants from drinking water, Adv. Mater. Sci. Eng. 2011 (2011) 1–17 (Article ID 872531).
[24] J. Wu, B. Li, J. Liao, Y. Feng, D. Zhang, J. Zhao, W. Wen, Y. Yang, N. Liu, Behavior and analysis of Cesium adsorption on montmorillonite mineral, J. Environ. Radioact. 100 (2009) 914–920.
[25] T.K. Huang, R. Wang, L. Shi, X.X. Lu, Montmorillonite K-10: An efficient and reusable catalyst for the synthesis of quinoxaline derivatives in water, Catal. Commun. 9 (2008) 1143–1147.
[26] W. Wan Ngah, L. Teong, M. Hanafiah, Adsorption of dyes and heavy metal ions by chitosan composites: A review, Carbohydr. Polym. 83 (2011) 1446–1456.
[27] F. Rasouli, S. Aber, D. Salari, A. Khataee, Optimized removal of Reactive Navy Blue SP-BR by organo-montmorillonite based adsorbents through central composite design. Appl. Clay Sci. 87 (2014) 228–234.
[28] L. Wang, A. Wang, Adsorption characteristics of Congo Red onto the chitosan/montmorillonite nanocomposite, J. Hazard. Mater. 147 (2007) 979–985.
[29] C.Y. Su, W.G. Li, X.Z. Liu, L. Zhang, Adsorption property of direct red brown onto acid-thermal-modified sepiolite and optimization of adsorption conditions using Box–Behnken response surface methodology, Desalin. Water Treat. 52 (2014) 880–888.
[30] Q. Jia, C.H. Xiong, X.Y. Chen, S.G. Zhou, C.P. Yao, C.N. Ma, Optimization of conditions for Cu(II) adsorption on 110 resin from aqueous solutions using response surface methodology and its mechanism study, Desalin. Water Treat. 51 (2013) 4613–4621.
[31] G.E. Box, J.S. Hunter, W.G. Hunter, Statistics for experimenters: Design, innovation, and discovery, John Wiley & Sons, Hoboken, NJ, 2005.
[32] R.H. Myers, C.M. Anderson-Cook, Response surface methodology: Process and product optimization using designed experiments, vol. 705, John Wiley & Sons, Hoboken, NJ, 2009.
[33] J. Zhang, L. Wang, A. Wang, Preparation and properties of chitosan-*g*-poly (acrylic acid)/montmorillonite superabsorbent nanocomposite via *in situ* intercalative polymerization, Ind. Eng. Chem. Res. 46 (2007) 2497–2502.
[34] C. Appel, L.Q. Ma, R. Dean Rhue, E. Kennelley, Point of zero charge determination in soils and minerals via traditional methods and detection of electroacoustic mobility, Geoderma 113 (2003) 77–93.
[35] M. Sathishkumar, S. Pavagadhi, K. Vijayaraghavan, R. Balasubramanian, S. Ong, Experimental studies on removal of microcystin-LR by peat, J. Hazard. Mater. 184 (2010) 417–424.
[36] W. Chow, Z. Mohd Ishak, J. Karger-Kocsis, A. Apostolov, U. Ishiaku, Compatibilizing effect of maleated polypropylene on the mechanical properties and morphology of injection molded polyamide 6/polypropylene/organoclay nanocomposites, Polymer 44 (2003) 7427–7440.
[37] Y. Fukushima, X-Ray diffraction study of aqueous montmorillonite emulsions, Clays Clay Miner. 32 (1984) 320.
[38] X. Wu, D. Zhao, S. Yang, Impact of solution chemistry conditions on the sorption behavior of Cu(II) on Lin'an montmorillonite, Desalination 269 (2011) 84–91.
[39] B. Tyagi, C.D. Chudasama, R.V. Jasra, Determination of structural modification in acid activated montmorillonite clay by FT-IR spectroscopy, Spectrochim. Acta, Part A 64 (2006) 273–278.
[40] M. Elibol, Response surface methodological approach for inclusion of perfluorocarbon in actinorhodin fermentation medium, Process Biochem. 38 (2002) 667–673.
[41] K. Yetilmezsoy, A. Saral, Stochastic modeling approaches based on neural network and linear-nonlinear regression techniques for the determination of single droplet collection efficiency of countercurrent spray towers, Environ. Model. Assess. 12 (2007) 13–26.
[42] H.L. Liu, Y.W. Lan, Y.C. Cheng, Optimal production of sulphuric acid by *Thiobacillus thiooxidans* using response surface methodology, Process Biochem. 39 (2004) 1953–1961.
[43] P. Pendleton, R. Schumann, S.H. Wong, Microcystin-LR adsorption by activated carbon, J. Colloid Interface Sci. 240 (2001) 1–8.

[44] P. de Maagd, A.J. Hendriks, W. Seinen, D.T. Sijm, pH-Dependent hydrophobicity of the cyanobacteria toxin microcystin-LR, Water Res. 33 (1999) 677–680.
[45] C.D. Tran, S. Duri, A. Delneri, M. Franko, Chitosan-cellulose composite materials: Preparation, characterization and application for removal of microcystin, J. Hazard. Mater. 252 (2013) 355–366.
[46] S.C. Chang, C.H. Li, J.J. Lin, Y.H. Li, M.R. Lee, Effective removal of *Microcystis aeruginosa* and microcystin-LR using nanosilicate platelets, Chemosphere 99 (2014) 49–55.
[47] H. Song, E.S. Reichwaldt, A. Ghadouani, Contribution of sediments in the removal of microcystin-LR from water, Toxicon 83 (2014) 84–90.
[48] X. Wu, B. Xiao, R. Li, C. Wang, J. Huang, Z. Wang, Mechanisms and factors affecting sorption of microcystins onto natural sediments, Environ. Sci. Technol. 45 (2011) 2641–2647.
[49] Y.-S. Ho, G. McKay, Pseudo-second order model for sorption processes, Process Biochem. 34 (1999) 451–465.
[50] H. Asfour, O. Fadali, M. Nassar, M. El-Geundi, Equilibrium studies on adsorption of basic dyes on hardwood, J. Chem. Technol. Biotechnol. 35 (1985) 21–27.
[51] M. Sathishkumar, A. Binupriya, D. Kavitha, S. Yun, Kinetic and isothermal studies on liquid-phase adsorption of 2,4-dichlorophenol by palm pith carbon, Bioresour. Technol. 98 (2007) 866–873.
[52] Y. Ho, J. Ng, G. McKay, Kinetics of pollutant sorption by biosorbents: Review, Sep. Purif. Rev. 29 (2000) 189–232.
[53] G. Boyd, A. Adamson, L. Myers Jr, The exchange adsorption of ions from aqueous solutions by organic zeolites. II. Kinetics 1, J. Am. Chem. Soc. 69 (1947) 2836–2848.
[54] W. Weber, J. Morris, Kinetics of adsorption on carbon from solution, J. Sanit. Eng. Div. Am. Soc. Civ. Eng. 89 (1963) 31–60.
[55] M. Sathishkumar, A.R. Binupriya, K. Vijayaraghavan, S.I. Yun, Two and three-parameter isothermal modeling for liquid-phase sorption of Procion Blue H-B by inactive mycelial biomass of *Panus fulvus*, J. Chem. Technol. Biotechnol. 82 (2007) 389–398.
[56] G. Newcombe, B. Nicholson, Water treatment options for dissolved cyanotoxins, J. Water Supply: Res. Technol. - AQUA 53 (2004) 227–239.
[57] Y. Deng, D. Qi, C. Deng, X. Zhang, D. Zhao, Superparamagnetic high-magnetization microspheres with an Fe_3O_4@SiO_2 core and perpendicularly aligned mesoporous SiO_2 shell for removal of microcystins, J. Am. Chem. Soc. 130 (2008) 28–29.
[58] H. Zhao, J.B. Qiu, H. Fan, A.F. Li, Mechanism and application of solid phase adsorption toxin tracking for monitoring microcystins, J. Chromatogr. A 1300 (2013) 159–164.
[59] W. Teng, Z.X. Wu, D. Feng, J.W. Fan, J.X. Wang, H. Wei, M.J. Song, D.Y. Zhao, Rapid and efficient removal of microcystins by ordered mesoporous silica, Environ. Sci. Technol. 47 (2013) 8633–8641.
[60] G. Güçlü, E. Al, S. Emik, T.B. İyim, S. Özgümüş, M. Özyürek, Removal of Cu^{2+} and Pb^{2+} ions from aqueous solutions by starch-graft-acrylic acid/montmorillonite superabsorbent nanocomposite hydrogels, Polym. Bull. 65 (2010) 333–346.